NANO · MICRO small
www.small-journal.com

An Electrodeposited MXene-$Ti_3C_2T_x$ Nanosheets Functionalized by Task-Specific Ionic Liquid for Simultaneous and Multiplexed Detection of Bladder Cancer Biomarkers

*Md. Sharifuzzaman, Sharat Chandra Barman, Md. Abu Zahed, Sudeep Sharma, Hyosang Yoon, Joong San Nah, Hyunsik Kim, and Jae Yeong Park**

Controlled deposition of 2D multilayered nanomaterials onto different electrodes to design a highly sensitive biosensing platform utilizing their active inherent electrochemistry is extremely challenging. Herein, a green, facile, and cost-effective one-pot deposition mechanism of 2D MXene-$Ti_3C_2T_x$ nanosheets (MXNSs) onto conductive electrodes within few minutes via electroplating (termed electroMXenition) is reported for the first time. The redox reaction in the colloidal MXNS solution under the effect of a constant applied potential generates an electric field, which drives the nanoparticles toward a specific electrode interface such that they are cathodically electroplated. A task-specific ionic liquid, that is, 4-amino-1-(4-formyl-benzyl) pyridinium bromide (AFBPB), is exploited as a multiplex host arena for the substantial immobilization of MXNSs and covalent binding of antibodies. A miniaturized, single-masked gold dual interdigitated microelectrode (DIDμE) is microfabricated and presented by investigating the benefit of AFBPB coated on MXNSs. The resulting MXNSs-AFBPB-film-modified DIDμE biosensor exhibited a 7× higher redox current than bare electrodes owing to the uniform deposition. Using Apo-A1 and NMP 22 as model bladder cancer analytes, this newly developed dual immunosensor demonstrated precise and large linear ranges over five orders of significance with limit of detection values as low as 0.3 and 0.7 pg mL^{-1}, respectively.

1. Introduction

In recent years, a unique class of 2D multilayered transition metal carbides (or carbonitrides) and nitrides (known as MXenes) has emerged rapidly and gained significant research attention since the advent of Ti_3C_2 in 2011.[1,2] Generally, MXenes (with chemical formula $M_{n+1}X_nT_x$, where M = transition metals such as Ti, Sc, V, Nb, Mo, and Cr; X = C and/or N; T_x = surface functional groups, such as −OH, −O, and minor −F; n = 1, 2, or 3) are synthesized by selectively etching A – group sp elements (typically group III A or IV A such as Al or Ga) from layered parent ternary MAX phases (with chemical formula Mn + 1AXn, where, A = elements from groups 13 and 14, such as Al, Ga, C, and Si).[3] To date, families of MXenes comprising more than 30 members have been successfully synthesized, such as Ti_2CT_x, V_2CT_x, Mo_2CT_x, and $Ti_3C_2T_x$.[3] Among them, MXene-$Ti_3C_2T_x$ nanosheets (MXNSs) is the most promising and well-studied candidate owing to its optimized synthesis, high metallic conductivity, high strength, high stability, excellent catalytic properties, and hydrophilicity with various surface functionalities.[1,4,5] Owing to its versatile chemistry, MXNSs is a promising candidate in a plethora of applications, including supercapacitors, energy storage,[6,7] electronics,[8] and catalysis,[5] In addition, MXNSs have recently emerged as excellent transducing electrode material in electrochemical biosensing owing to its active inherent electrochemistry compared with other 2D nanomaterials. Hitherto, several biosensors based on MXNSs have been utilized for the detection of prostate specific antigen,[9] phenol,[10] microRNA-182,[11] glucose,[12] acetaminophen, and isoniazid.[13]

In the fabrication of advanced biosensors, the most challenging issue of arranging nanomaterials into a particular position on a patterned electrode with controlled architecture, morphology, and thickness should be solved. Many chemicals, as well as physical deposition techniques, have been established to assemble 2D nanomaterials (graphene, CNT, MoS_2, and MXene) over electrodes. Currently, the most popular approaches for assembling 2D nanomaterials onto electrodes for sensing rely on chemical deposition techniques, for example, layer-by-layer assembly,[14,15] spin coating,[16] inkjet printing,[17] spray coating,[18] vacuum filtration,[19] and

Md. Sharifuzzaman, S. C. Barman, Md. A. Zahed, S. Sharma, H. Yoon, J. S. Nah, H. Kim, Prof. J. Y. Park
Department of Electronic Engineering
Advanced Sensor and Energy Research Laboratory
Kwangwoon University
447-1, Seoul 139-701, Republic of Korea
E-mail: jaepark@kw.ac.kr

The ORCID identification number(s) for the author(s) of this article can be found under https://doi.org/10.1002/smll.202002517.

DOI: 10.1002/smll.202002517

drop-casting.[20] Among them, drop-casting is the most popular and widely used technique for assembling nanomaterials because it is a facile, economical, and time-saving technique.

For the inherent utilization of 2D MXNSs as electrode material in sensors, supercapacitors, solar cells, electronics, optoelectronics, and many other devices, various solution-based deposition techniques have been investigated to fabricate uniform and highly conductive thin films or coatings. Typically, 2D MXNSs on electrodes of electrochemical sensors are assembled using the conventional drop-casting process.[9,11–13] This process, although efficient, has intrinsic and recalcitrant shortcomings, such as insufficient film thickness control, morphology change, presence of toxic materials, coffee ring effect, and loss of active surface area and functional groups.[21,22] Hence, poor sensing performance results when detecting low concentration biomarkers and their long-term reproducibility is limited. In addition, the precise deposition of homogeneous MXNSs on conductive substrates patterned with different electrode geometries, such as circular, square, needle, and interdigitated (IDE) remains scientifically challenging. Therefore, a facile, precise, and controlled method of depositing 2D MXNSs onto the desired pattern electrodes is highly necessitated. However, this has not been described in any previous findings.

Among the well-known wet chemical deposition techniques, one method that satisfies all the requirements for the integration of MXNSs with substrates patterned with different electrode geometries is the electrochemical deposition. Recent studies have revealed that 2D materials, such as GO, MoS_2, and CNT can be easily deposited onto a specific electrode substrate with controlled film morphology and thickness via the electrodeposition method.[21,23,24] Generally, MXNSs have high, negative zeta potentials owing to the surface terminal groups (such as −F, −OH, and −O), which afford their hydrophilic nature and render them suitable for forming stable colloids containing few-layer MXNSs in various polar solvents.[25] Additionally, redox-capable transition metal layers on the surface of MXNSs enable the latter to be used in the electrochemical deposition method.[26] Therefore, the electrochemical deposition of MXNSs on specific patterned electrodes with controlled thickness may be one of the most intriguing methods for obtaining large-scale and high-quality MXNS thin films. ElectroMXenition can occur in two steps, in which the MXene nanoparticles migrate toward the working interface under the effect of an electric force resulting from redox cycles, followed by their deposition to form a homogeneous MXNS film.

Ionic liquids (ILs), with its intriguing properties such as excellent ionic conductivity; wide solubility range; zero vapor pressure; high chemical, thermal, and redox stability; and excellent biocompatibility, offer a plethora of design combinations by modifying the properties of both organic cations and inorganic anions independently.[27–29] This modification or functionalization of ILs (known as "task-specific ionic liquids—TSILs") has enabled versatile physicochemical properties, which are suitable for specific applications. Hitherto, aldehyde functionalized ILs (CHO-IL) have been used frequently for the fabrication of ultrasensitive sensors and biosensors.[30–32] The aldehydic group of IL can serve as a host for attaching enzymes, biomolecules, and antibodies directly. However, the electrode surface modification or sorption affinity between transducing materials (GO, CNT, MoS_2, and MXNSs) and ILs through simple physical interactions always suffers from poor stability and sensitivity. Therefore, multifunctional TSILs comprising different cations (4-aminopyridine) and anions (4-(bromomethyl)-benzaldehyde) forming 4-amino-1-(4-formyl-benzyl) pyridinium bromide (AFBPB) are a possible solution. The aldehydic groups of AFBPB can directly capture enzymes or biomolecules through a strong covalent bond.[31] In addition, the amine groups ($-NH_2$) of AFBPB can bind strongly with the hydroxyl −OH groups of MXNSs through electrostatic interactions and π–π stacking.[33,34] To the best of our knowledge, studies regarding multifunctional TSIL (AFBPB)-based immunosensing tags in the development of sensors or biosensors have not been published.

Miniaturized advanced electrochemical biosensors employing the IDE microelectrode array configuration is a geometry of interest for ultrasensitive point-of-care applications owing to its signal-transducing capability by enhanced redox cycling between adjacent comb-shaped electrode pairs.[35] Although challenging, the specific and stable modification of electrode arrays using 2D and 3D transducing nanomaterials is necessitated to utilize the enhanced redox cycling effect of IDEs for electrochemical sensors. Therefore, the suitable modification method, electrode design geometry, and system are key in circumventing the aforementioned challenges.

We herein report a green, facile, and cost-effective one-pot deposition mechanism of 2D MXNSs for developing high-performance electrochemical biosensors via electroplating technique (termed electroMXenition) for the first time (**Figure 1**A–C). The deposition uniformity of MXNSs at room temperature under different electroMXenition times, with optimized concentration and constant voltage, was carefully investigated (Figure 1D). MXNSs ($Ti_3C_2T_x$) were carefully synthesized by the optimized minimally intensive layer delamination (MILD) method,[2] which involved the selective etching of aluminum layers from its precursor MAX phases (Ti_3AlC_2) (**Figure 2**A). Furthermore, a TSIL, that is, AFBPB, comprising cation (4-aminopyridine) and anion (4-(bromomethyl)-benzaldehyde) was synthesized and implemented on the surface of MXNSs to fabricate a model bio-electrochemical dual-sensing platform (Figure 2B,C,D). The aldehydic groups of AFBPB can directly capture the enzymes or biomolecules through a strong covalent bond. Additionally, the amine groups of AFBPB bind strongly with the hydroxyl −OH groups of MXNSs through electrostatic interactions and π–π stacking.

As a proof of concept, two model protein biomarkers in urine related to bladder cancer (Apo-A1 and NMP 22) progression were tested using the newly designed dual immunosensor. The fabricated device is characterized and evaluated by measuring its sensitivity, selectivity, and reproducibility with a limit of detection (LOD) values to meet clinical requirements.

2. Results and Discussion

2.1. Electroplating Technique of MXNSs–ElectroMXenition

Figure 1A shows the schematic diagram of a customized electrolyte bath and the electroMXenition process.

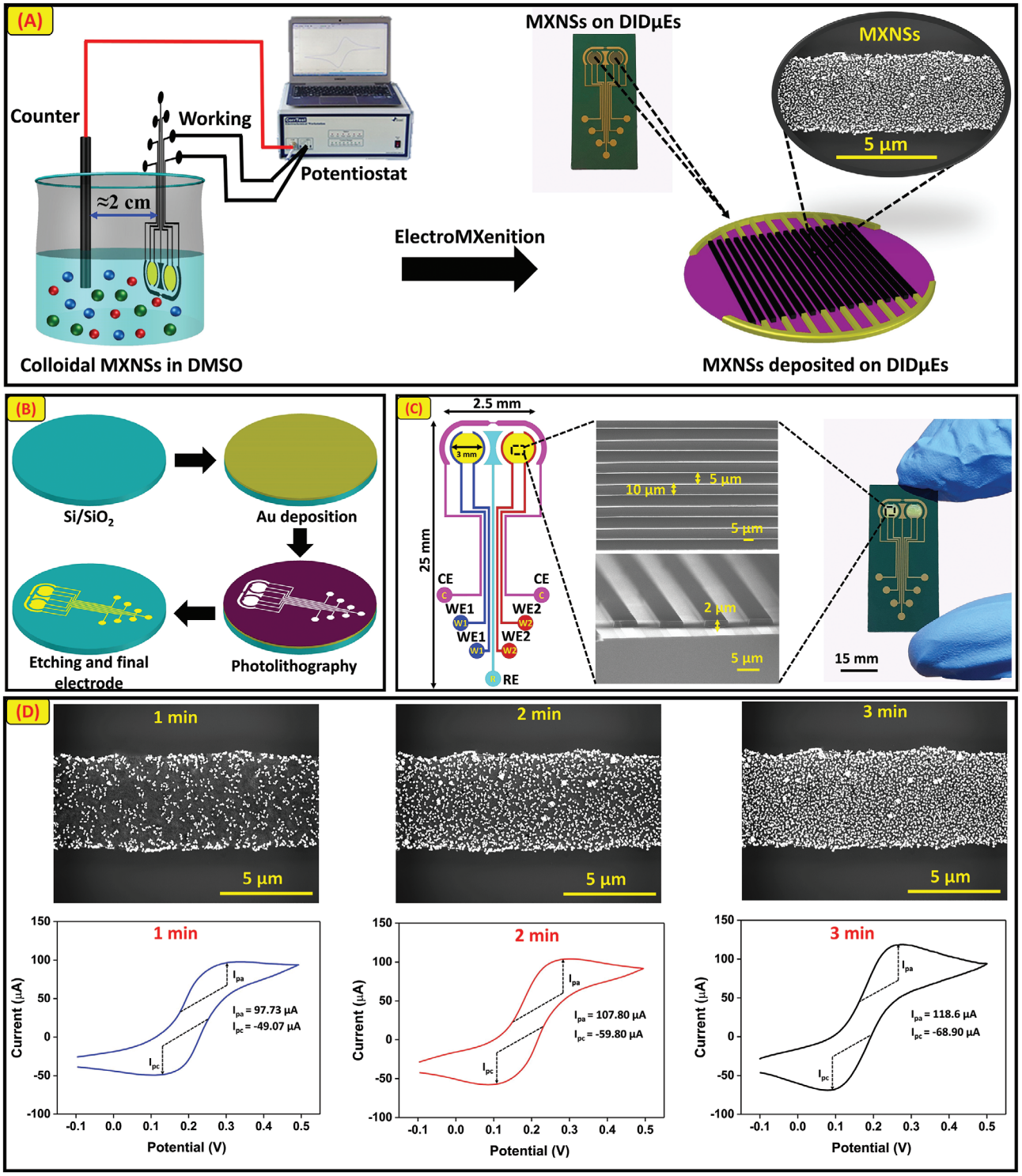

Figure 1. A) Schematic illustration of the customized electrolyte bath and the electroMXenition process. B) Standard single-masked UV photolithography and etching procedures to fabricate DIDµE. C) Mapping of the sensor, an optical image of the real sensor, and FESEM images of the top and cross-sectional views of the interdigitated patterns. D) Uniformity and redox performance analysis of the MXNSs onto DIDµEs at room temperature using FESEM and CV (in 5 mM K_3/K_4 solution) under different electroMXenition times (1–3 min), with optimized concentration and constant voltage.

Premicrofabricated conductive gold dual interdigitated microelectrodes (DIDµEs) and flexible indium tin oxide (ITO) electrode (See Figure 1B and Figure S4, Supporting Information) were used as a working electrode on which electroMXenition was performed, whereas a Pt rod was selected as a counter electrode. These two electrodes at a distance of ≈2 cm were dipped

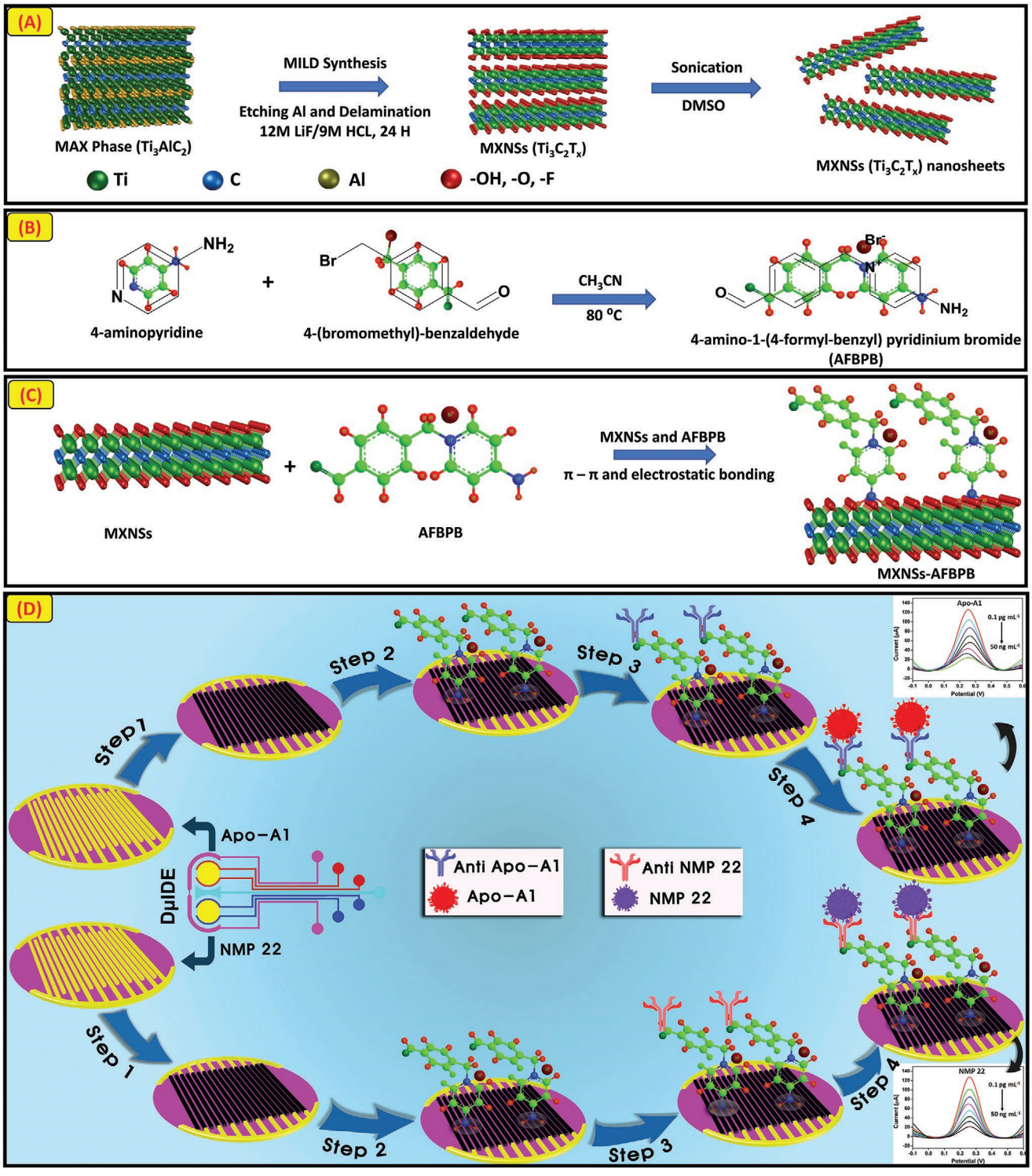

Figure 2. A) Schematic illustration of the MXNSs-$Ti_3C_2T_x$ synthesis procedure. B) Schematic illustration of multifunctional 4-amino-1-(4-formyl-benzyl) pyridinium bromide (AFBPB) TSIL synthesis procedure. C) Schematic illustration of MXNS functionalization using AFBPB. D) Schematic illustration of the different steps involved in the fabrication of the immunosensor for Apo-A1 and NMP 22 detection.

in parallel into an aqueous solution of dimethyl sulfoxide (DMSO) containing colloidal MXNSs ($Ti_3C_2T_x$) as an electrolyte. The MXNSs dispersed completely and were highly stable in organic solvent DMSO (Figure S1, Supporting Information) owing to their hydrophilic nature and highly negative zeta (ζ) potential in the range of –40 to –70 mV.[25] The appropriate viscosity and dispersibility rendered DMSO suitable for suspending MXNSs. Furthermore, its slow evaporation rate

enabled a timely arrangement of the nanosheets on the electrodes after the nanosheets were dispersed uniformly.

$$Ti_3C_2 \xrightarrow{\text{In water}} Ti_3C_2(OH)_2 + H_2 \quad (1)$$

The overall resistance (R_T) of the external circuit of the system can be calculated using the following equation.[24]

$$R_T = \frac{V}{I} = R_{EB} + R_C \quad (2)$$

where R_T is the total resistance of the external circuit; V and I are the applied voltage and current, respectively; R_{EB} is the electrolyte bath resistance associated with the electrolyte's concentration and the densities of related ions in solution; R_C is the total contact resistance at the DIDμEs and Pt rod electrode, which primarily depend on the electrode configuration, including the distance between electrodes and the effective reaction area. As such, the value of R_T may vary over time and hence extremely difficult to control. Therefore, a constant voltage source was maintained during the electroMXenition to circumvent the unstable variables.

Under a constant applied potential, a redox reaction occurred in the colloidal MXNS suspension. This phenomenon eventually generated an electric field that caused the nanoparticles to gather near the electrode interface; finally, they were cathodically electrodeposited onto the specific electrodes to form crystalline MXNSs. Moreover, the evolution of gas bubbles at the cathode during electroMXenition ensured the deposition of MXNSs on the electrodes.

During electroMXenition, the assumed overall redox reaction in the electrolytic solution for the formation of crystalline MXNSs (Ti_3C_2) can be expressed as follows:

$$Ti_3C_2 + H_2O \rightarrow 3Ti^{3+} + CO + C + 2H^+ + 11e^- \quad (3)$$

$$Ti_3C_2 + 7H_2O \rightarrow 3TiO_2^{2+} + CO + C + 14H^+ + 20e^- \quad (4)$$

$$Ti^{4+} + e^- = Ti^{3+} \quad (5)$$

$$Ti^{3+} + 3e^- = Ti \quad (6)$$

According to the reaction above, the Ti^{4+} species can be reduced to Ti^{3+} on the working electrode, and the elemental carbon can serve as a carbide source for the crystallization of $Ti_3C_2T_x$. Some C atoms may lose due to the evolution of CO or CO_2 during the anodic dissolution of Ti_3C_2.[36] During reaction, Ti_3C_2 produces Ti^{3+} and CO as primary products, then Ti^{3+} undergoes immediate oxidation at the electrode interfaces whereas CO may either oxidized to CO_2 or desorb.[36] Moreover, oxidation of Ti_3C_2 may produce some TiO_2 anatase.[37] The formation of crystalline $Ti_3C_2T_x$ was further revealed from field emission scanning electron microscopy (FESEM), transmission electron microscopy (TEM), energy dispersive spectrometry (EDS), X-ray diffraction (XRD), Fourier-transform infrared spectroscopy (FTIR), X-ray photoelectron spectroscopy (XPS), and Raman spectroscopy as will be described in the Experimental Section and Supporting Information.

To analyze the dependence of the MXNS uniformity (U) on the electroMXenition parameters, the following expression was used:

$$U \equiv \text{Function}(\pm, C, V, t) \quad (7)$$

where ± represents the counter and working electrode, C is the concentration of the electrolyte (colloidal MXNSs in DMSO), V is the constant applied voltage, and t is the electroMXenition time. We investigated the deposition uniformity of the MXNSs at room temperature under different electroMXenition times of 1, 2, and 3 min, with an optimized concentration (2 mg mL^{-1}), and constant voltage. The homogeneity and uniformity of the MXNSs increased successively with the electroMXenition time (t), as shown in Figure 1D. Figure S4, Supporting Information, indicates that the color of the ITO films became darker when the electroMXenition time (t) increased. Figure S5A–D, Supporting Information, shows the optical image of the as-deposited MXNSs on the ITO electrode for 3 min and their corresponding low and high-resolution FESEM images of the as-deposited MXNSs. However, to avoid an electrical connection between the two combs, the deposition time (t) was limited to 3 min. The uniformity and redox performance of the MXNSs onto the DIDμEs was evaluated using FESEM and cyclic voltammetry (CV) (in 5 mM K_3/K_4 solution), as shown in Figure 1D. The redox current for the 1 min deposited DIDμEs was comparatively lower than that of the 2 min deposited electrode as the uniformity of the MXNSs for 1 min was lower than that for 2 min. On the contrary, the 3 min deposited DIDμEs exhibited the highest redox current owing to the best uniform deposition of MXNSs. Finally, we selected the 3 min electroMXenition time for the uniform and conformal deposition of MXNSs on specific DIDμEs.

2.2. Materials Characterization (As-Deposited MXNSs and Post-Treated MXNSs–AFBPB)

The as-deposited homogeneous MXNSs and MXNSs–AFBPB-modified DIDμEs were characterized by FESEM, TEM, EDS, XRD, FTIR, and XPS. The successful synthesis of multifunctional AFBPB TSILs was confirmed and characterized by ^1H and ^{13}C NMR using ChemDraw software (Figures S2 and S3, Supporting Information). The chemical interaction between MXNSs and AFBPB was further analyzed by Raman spectroscopy (Figure S8, Supporting Information). We also demonstrated the advantage of the present deposition method of MXNSs as compared to other methods, drop-casting and electrophoretic deposition method (EPD) (in terms of film structure, morphology, the orientation of MXene flakes, chemical composition, electrochemical performances, etc.), through experimental results (Figures S7 and S9, Supporting Information).

The conformal deposition and morphologies of MXNSs and AFBPB onto DIDμEs were characterized using FESEM analysis (**Figure 3**A–F). After electroMXenition for 3 min, the surface of the DIDμEs became darker and rougher owing to the uniform deposition of MXNSs onto DIDμEs. From the zoom views of the MXNS-deposited DIDμEs marked by the rectangle in Figure 3A–E, one can distinctly observe that the nanosheets are uniformly deposited on each specific comb. The high magnification image (Figure 3E) exhibits the loose multilayered accordion-like structure of MXNSs-$Ti_3C_2T_x$ and the average thickness of the MXNS layers is less than 40 nm.[38] After an AFBPB deposition (Figure 3F) on the

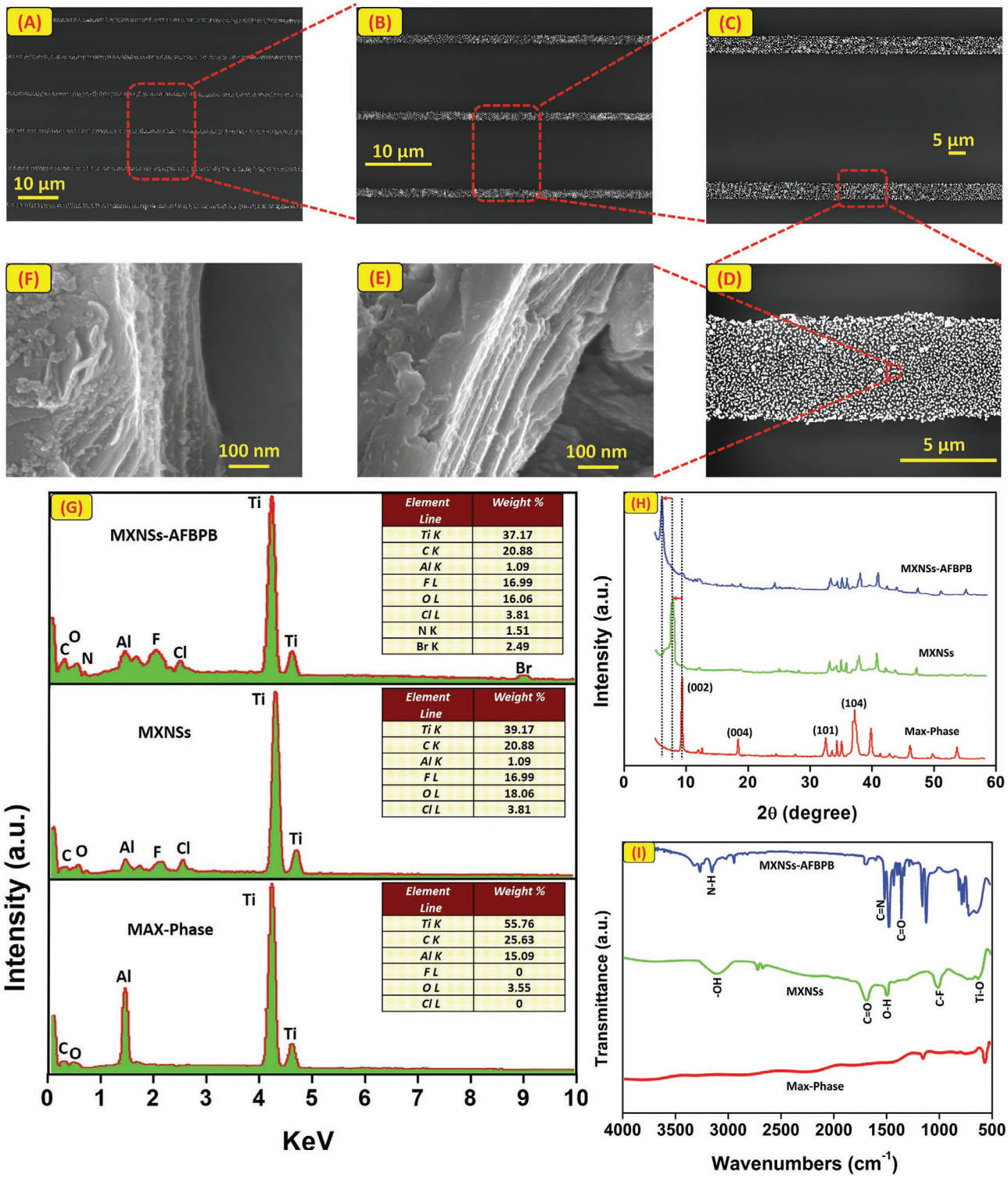

Figure 3. A–E) Low- and high-magnification FESEM images of MXNSs on DIDµEs. F) High-resolution FESEM image of TSIL AFBPB (4-amino-1-(4-formyl-benzyl) pyridinium bromide) onto MXNSs. G) EDS spectra and elemental weight percentage analysis of MAX phase (Ti_3AlC_2), MXNSs ($Ti_3C_2T_x$), and MXNS–AFBPB. H) XRD pattern analysis of MAX phase (Ti_3AlC_2), MXNSs ($Ti_3C_2T_x$), and MXNS–AFBPB. I) FTIR spectra analysis of MAX phase (Ti_3AlC_2), MXNSs ($Ti_3C_2T_x$), and MXNS–AFBPB.

MXNSs, the IL nanoparticles (less than 20 nm) are uniformly distributed between the $Ti_3C_2T_x$ multilayer and surface. It is noteworthy that the deposition of AFBPB with excellent ionic conductivity and biocompatibility can serve as a multiple host platform for a substantial bonding with biomolecules and MXNSs.

The existence of compositional elements and their weight percentages in the as-deposited MXNSs and MXNSs-AFBPB were characterized by EDS analysis (Figure 3G).

The parent MAX phases (Ti_3AlC_2) exhibited a distinct aluminum (Al) peak (15.09%). After a successful etching, the Al peak (1.09%) nearly vanished and the element fluorine (F) (16.99%) occurred; moreover, the percentage of oxygen (O) increased in the as-deposited MXNSs ($Ti_3C_2T_x$). By contrast, the EDS spectra of MXNSs–AFBPB exhibited the additional peaks of nitrogen (N) (1.51%) and bromine (Br) (2.49%), implying the grafting of $-NH_2$ on the as-deposited MXNSs resulting from AFBPB.

The conformal deposition and crystal structure of the as-deposited MXNSs and post-treated MXNSs–AFBPB films were also confirmed by XRD analysis (Figure 3H). The disappearance of the intense XRD peak of the MAX phases (Ti_3AlC_2) at a 2θ of 38.6° suggested the etching of Al layers in the as-deposited MXNSs.[39] Meanwhile, the (002) peak of the as-deposited MXNSs lost its intensity and shifted to lower angles (9.5° to 7.3°) owing to the loss of crystallinity and the increase in d-spacing.[9] Moreover, after the introduction of AFBPB in MXNSs, the 2θ angle shifted to 6.5°, demonstrating the successful bonding between the $-NH_2$ group of AFBPB and MXNSs.

After the etching and exfoliation of the MAX phase (Ti_3AlC_2), the FTIR spectra (Figure 3I) of the as-deposited MXNSs ($Ti_3C_2T_x$) showed the major characteristic bands at 3240 (−OH), 1704 (C=O), 1490 (O−H), 1050 (C−F), and 670 cm^{-1} (Ti−O) respectively, which agreed well with findings in previous studies.[40,41] In the case of MXNSs-AFBPB, two intense peaks at 1420 and 3210 cm^{-1} corresponded to the free aldehydic (−C=O) and bending amine groups (−N−H) of the AFBPB, respectively. Moreover, the peak at 1680 cm^{-1} indicated the formation of an imine bond (−C=N) between the $-NH_2$ and −OH groups of AFBPB and the MXNSs, respectively, through electrostatic interactions and π–π stacking.[31] This indicated that AFBPB was successfully grafted on the as-deposited MXNSs.

High-resolution XPS was utilized to characterize the chemical and valence states of the as-deposited MXNSs ($Ti_3C_2T_x$) and MXNSs-AFBPB (**Figure 4**A–F). The wide survey scans of MXNSs (Figure 4A) exhibited the existence of O and F along with the core constituent elements Ti and C, indicating the possible surface functionalization during etching and exfoliation. By contrast, the XPS survey scans of MXNSs–AFBPB indicated the presence of Br, N, O, F, Ti, and C, suggesting the uniform distribution of AFBPB on the MXNSs. The presence of N 1s and Br 3d peaks in MXNSs-AFBPB confirmed the grafting of AFBPB on MXNSs (Figure 4B,C). The deconvoluted C 1 s spectra of the MAX phase (Figure 4D) can be obtained by fitting six binding energies at 280.44 (C−Ti), 282.01 (C−Ti−O), 284.14 (C−C), 285.66 (C−O), 287.94 (C−Al), and 289.46 eV (C−F).[9] After etching, the peak at 287.94 eV corresponding to the C−Al group almost disappeared in the as-deposited MXNSs (Figure 4E). In the C 1s spectrum of MXNSs-AFBPB (Figure 4F), the intensity of the C−Ti peak decreases, whereas a new peak at 286.26 eV was observed for C−N owing to the successful amidation reaction between AFBPB and the MXNSs. Furthermore, the predominant peak located at 286.26 eV for C−OH confirmed the presence of free aldehydic groups in MXNSs-AFBPB.

The high-resolution scans of the Ti 2p core level of the as-deposited MXNSs (Figure S6, Supporting information) can be deconvoluted with two sets of doublets, Ti $2p_{3/2}$ and Ti $2p_{1/2}$, separated by 10 eV. The high-resolution Ti $2p_{3/2}$ region combined with four peaks at 455.23, 457.11, 459.06, and 461.03 eV correspond to Ti−C (Ti^+), Ti−X (Ti^{2+}), Ti_xO_y (Ti^{3+}), and TiO_2 (Ti^{4+}), respectively.[42] By contrast, the Ti $2p_{1/2}$ region associated with $C-Ti-O_x$ and Ti−O groups were located at 462.91 and 464.86 eV, respectively.[43]

2.3. Fabrication and Characterization of Dual Immunosensor Utilizing MXNSs–AFBPB Bioconjugates

The design of miniaturized and highly sensitive electrochemical biosensors for multiplexed analysis can be varied based on fabrication strategy, geometry, and detection requirements. Therefore, to satisfy the requirements for detecting two cancer biomarkers simultaneously with the advantage of an IDE geometry for enhancing sensitivity and detection limits, the biosensor was fabricated elaborately. The DIDμEs were fabricated on a Si/SiO_2 substrate by standard photolithography and etching processes (Figure 1B), which are briefly described in the Experimental Section. The gold DIDμEs measured 25 mm × 2.5 mm × 0.002 mm with two circular-IDE working electrodes (each 3 mm-Ø) including one common counter and a reference electrode. Each working electrode was composed of 190 pairs of IDE gold electrodes (5/10 μm, electrode width/gap). A photograph of the fabricated DIDμE biosensor and the FESEM images of the top and cross-sectional views of the IDE patterns are shown in Figure 1C. To enhance the performance of the DIDμEs for the simultaneous detection of Apo-A1 (W1) and NMP 22 (W2), various transducing materials and biomolecules were integrated to embellish the sensing interface. More importantly, the MXNSs were first deposited via electroMXenition to enhance the active interface of the electrode and increase the simultaneous redox reaction between the adjacent combs. For the direct immobilization of enzymes in the immunosensor, AFBPB, a multifunctional TSIL, was loaded to the surface of the MXNSs by π–π and electrostatic absorption, which enhanced the ionic conductivity and biocompatibility. The MXNSs inherited many surface functional groups (−OH, −O, and −F); therefore, the negatively charged surface bonded with the positively charged amine groups of AFBPB. Meanwhile, the free aldehydic groups (−CHO) of AFBPB directly captured the enzymes or biomolecules through a strong covalent bond. Finally, Apo-A1 and NMP 22 antibodies were immobilized separately on the surface of MXNSs–AFBPB nanocomposites to form W1/MXNSs–AFBPB/Apo-A1 (immunosensor for Apo-A1 determination) and W2/MXNSs-AFBPB/NMP 22 (immunosensor for NMP 22 determination) bioconjugates for immunosensors. The different steps involved in the construction and functioning of the dual Apo-A1 and NMP 22 immunosensor was characterized by CV and electrochemical impedance spectroscopy (EIS) in 5 mM K_3/K_4, and the results and discussions are provided in the Section 2.3.2.

2.3.1. Optimization of Sensing Conditions

Figure 5A shows the exact measurement and sensing setup of the DIDμE biosensor in PBS (pH 7.4) containing a 5.0 mM k_3/K_4 solution.

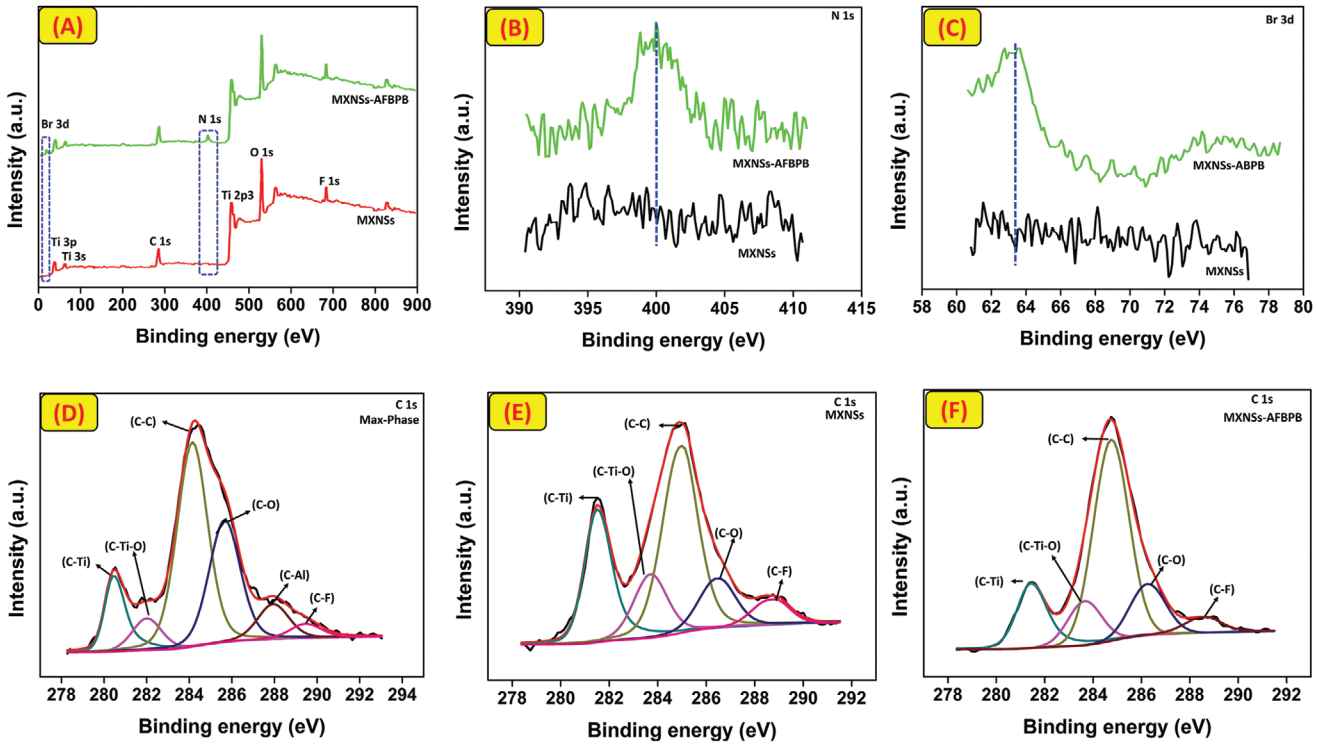

Figure 4. A) Survey XPS spectra of MXNSs and MXNSs–AFBPB. B) High-resolution N1s spectra of MXNSs and MXNSs–AFBPB. C) High-resolution Br 3d spectra of MXNSs and MXNSs–AFBPB. D) C1s spectra of MAX phase. E) C1s spectra of MXNSs. F) C1s spectra of MXNS–AFBPB.

The pH value of PBS affected the electro-analytical behavior of the immunosensors significantly. Therefore, to confirm the optimized pH, a series of PBS with various pH values ranging from 5.5 to 8.5 was investigated (Figure 5B). The results implied that PBS at pH = 7.4 exhibited the best electrochemical performance. Hence, PBS at pH = 7.4 was adapted for the following electrochemical experiments throughout this study.

The concentration of the AFBPB-loading solution on the surface of the MXNSs is critical as it affects antibody immobilization and the electro-analytical performance. Hence, differential pulse voltammetry (DPV) responses were observed by loading different concentrations of AFBPB (Figure 5C). The DPV currents of the immunosensor increased exponentially with the increasing concentration of AFBPB until the loading concentration reached 5 mg mL^{-1}; subsequently, the current began decreasing owing to the agglomeration of IL, resulting in a limited electron transfer on the working interface. Moreover, excess concentrations of the AFBPB-loading solution resulted in a higher background signal and therefore decreased the sensing accuracy and sensitivity of the immunosensors. Hence, 5 mg mL^{-1} of AFBPB-loading solution was selected as the optimal concentration for constructing the immunosensors.

The effect of the immunoreaction time for the formation of an antigen–antibody immunocomplex is an essential parameter affecting the sensitivity and selectivity of the immunosensors. As shown in Figure 5D,E, the DPV responses for Apo-A1 and NMP 22 decreased linearly from 5 to 40 min because the appropriate reaction between the antigen–antibody forming immunocomplex would consume some time. After 40 min, the responses of both immunosensors saturated. Hence, 40 min was finalized as a sufficient immunoreaction time for both Apo-A1 and NMP 22.

2.3.2. Electrochemical Characterization of DIDμE Immunosensors

The different function and modification steps included in the fabrication of the dual immunosensors were investigated through CV and EIS using PBS (pH 7.4) containing a 5.0 mM k_3/K_4 solution as a redox marker, and the results are shown in Figure 5F–I. After electroMXenition, the redox peak currents at W1 and W2 (Figure 5F,G, curve b) increased by almost 5× over bare electrodes (Figure 5F,G, curve a). This illustrates that the highly conductive accordion-like expanded layers of the MXNSs extended the active surface area and facilitated electron transfer at the interface of the electrode simultaneously. After the loading of AFBPB on the MXNSs (Figure 5F,G, curve c), the redox peaks further increased by 2×, implying that the grafting of AFBPB on the MXNSs enhanced the synergistic electrochemical effect. With the consecutive deposition of anti-Apo A1 and anti-NMP 22 on both electrodes (Figure 5F,G, curve d) followed by BSA immobilization (Figure 5F,G, curve e), the peak currents decreased because the surface of the electrodes was oriented by the insulating enzyme and protein, hence hindering the electron transfer in the interface of the electrode.[44] When Apo A1(1 ng mL^{-1}) and NMP 22 (1 ng mL^{-1}) were combined with the associated antibody, the redox peak currents decreased significantly (Figure 5F,G, curve f), suggesting the successful fabrication of the immunosensors.[45]

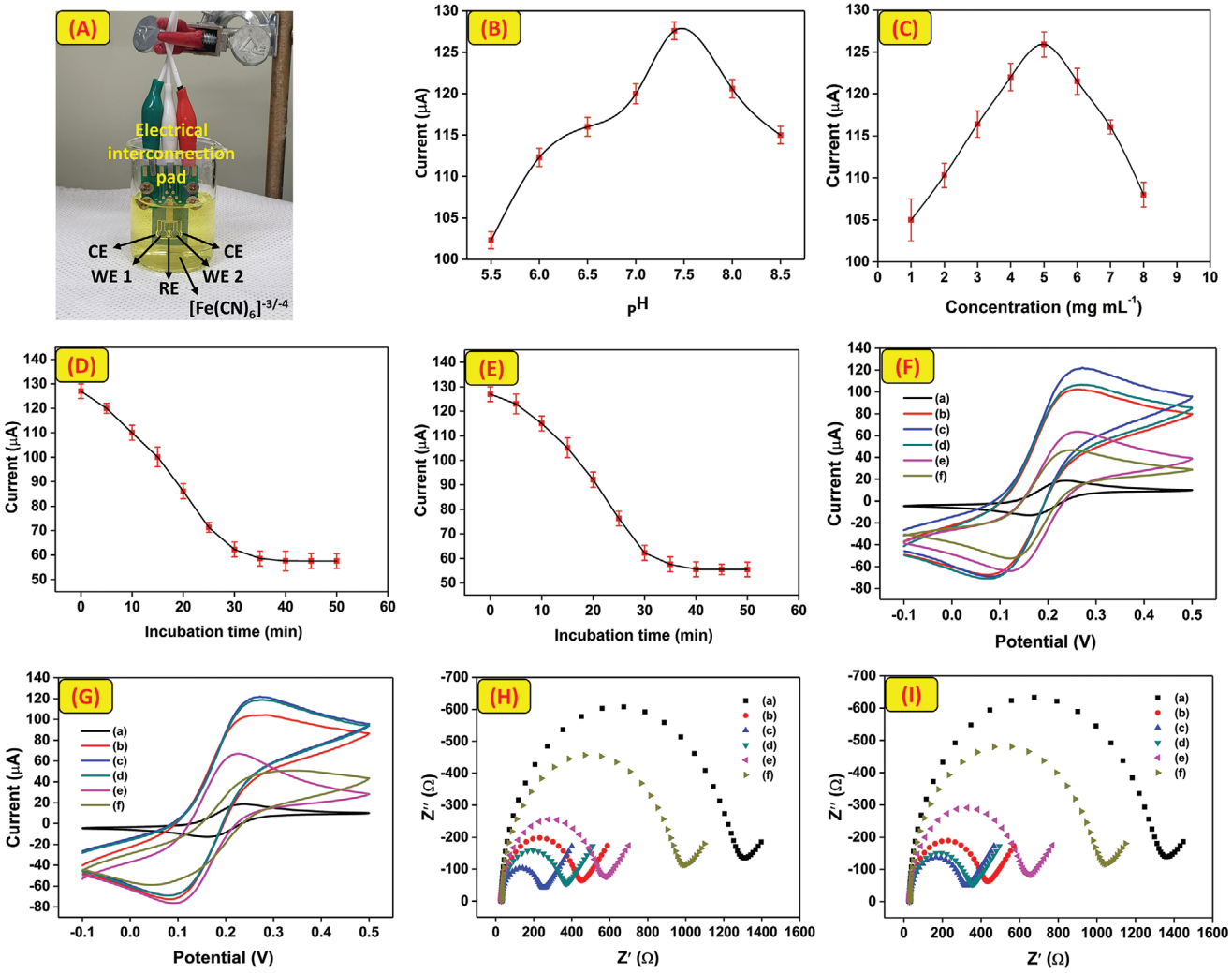

Figure 5. A) Measurement setup of the dual immunosensor in PBS (pH 7.4) containing 5.0 mM k_3/K_4 redox solution. B) pH value optimization. C) Loading concentration optimization of AFBPB onto MXNSs. D) Incubation time optimization for Apo-A1 (W1). E) Incubation time optimization for NMP 22 (W2). F) CVs of different fabrication steps for electrode W1, Apo-A1: a) DIDμEs, b) DIDμEs/MXNSs, c) DIDμEs/MXNSs–AFBPB, d) DIDμEs/MXNSs–AFBPB/Anti-Apo-A1, e) DIDμEs/MXNSs–AFBPB/Anti-Apo-A1/BSA, and f) DIDμEs/MXNSs–AFBPB/Anti-Apo-A1/BSA/Apo-A1. G) CV of different fabrication steps for W2, NMP 22: a) DIDμEs, b) DIDμEs/MXNSs, c) DIDμEs/MXNSs–AFBPB, d) DIDμEs/MXNSs–AFBPB/anti-NMP 22, e) DIDμEs/MXNSs–AFBPB/anti-NMP 22/BSA, and f) DIDμEs/MXNSs–AFBPB/anti-NMP 22/BSA/NMP22. H) EIS of different fabrication steps for electrode W1, Apo-A1: a) DIDμEs, b) DIDμEs/MXNSs, c) DIDμEs/MXNSs–AFBPB, d) DIDμEs/MXNSs–AFBPB/Anti-Apo-A1, e) DIDμEs/MXNSs–AFBPB/Anti-Apo-A1/BSA, and f) DIDμEs/MXNSs-AFBPB/Anti-Apo-A1/BSA/Apo-A1. I) EIS of different fabrication steps for W2, NMP 22: a) DIDμEs, b) DIDμEs/MXNSs, c) DIDμEs/MXNSs–AFBPB, d) DIDμEs/MXNSs–AFBPB/anti-NMP 22, e) DIDμEs/MXNSs–AFBPB/anti-NMP 22/BSA, and f) DIDμEs/MXNSs–AFBPB/anti-NMP 22/BSA/NMP22.

The interfacial physicochemical interactions included in each fabrication step of the dual immunosensor was further explored by EIS (Figure 5H,I). The diameter of the semicircle Nyquist plot represents the interface resistance (R_i) of the electrode.[46] The bare W1 and W2 (Figure 5H,I, curve a) showed large semicircle Nyquist plots with R_i of 1397 and 1447 Ω, respectively. After electroMXenition, R_i at W1 and W2 (Figure 5H,I, curve b) decreased significantly to 586.5 and 569.5 Ω, respectively, which can be ascribed to the excellent electro-conductibility of the MXNSs. When AFBPB was assembled on both electrodes (Figure 5H,I, curve c), R_i decreased slightly to 400.6 and 466.9 Ω, respectively, suggesting that AFBPB could also enhance the electron transfer. The subsequent deposition of anti-Apo A1 and anti-NMP 22 on both electrodes (Figure 5F,G, curve d) yielded higher R_i of 494.8 and 509.8 Ω, respectively, implying the successful decoration of the antibody; R_i increased successively to 699.2 and 769.1 Ω, respectively, when the electrodes were further modified using BSA (Figure 5H,I, curve e). However, when Apo A1(1 ng mL^{-1}) and NMP 22 (1 ng mL^{-1}) were immobilized (Figure 5H,I, curve f), R_i increased significantly to 1098.3 and 1148.7 Ω, respectively, confirming the successful construction of the immunosensors.[46]

The consistent results of CV and EIS demonstrated the successful fabrication of the dual immunosensors for the simultaneous detection of Apo A1 and NMP 22.

2.3.3. Simultaneous Detection of Apo-A1 and NMP 22

To detect the ultrasensitive immunoreaction between the antibody and antigen on the as-fabricated dual immunosensors, DPV was employed as it is the most sensitive and advanced technique compared with other analytical techniques. Under ideal conditions, where the background response is stable, the DPV currents in the (PBS, pH 7.4 + 5.0 mM k_3/K_4) redox marker for the simultaneous detection of Apo-A1 and NMP 22 on the immunosensors (W1 and W2) decreased with increasing concentrations of antigens owing to the insulating immunocomplex layer on the working electrodes (**Figure 6**A,C). Both calibration graphs show negative collinear relationships between the DPV peak currents and the $\log_{10}$ concentrations of the analytes ranging from 0.1 pg mL^{-1} to 50 ng mL^{-1} with the regression coefficients (R^2) of 0.997 and 0.995 for Apo-A1 and NMP 22, respectively (Figure 6B,D, respectively). The calculated LOD values for Apo-A1 and NMP 22 were 0.3 and 0.7 pg mL^{-1} at a signal-to-noise ratio of 3, respectively, which were approximately five orders of magnitude lower than the clinically acceptable level in human urine.[47,48] The superior electro-analytical performance, including ultralow LOD values and large linear ranges for multiplexed analysis, render the specially designed DIDμE immunosensors extremely promising in practical applications compared with previously reported immunosensors (Tables S1 and S2, Supporting Information,).

2.3.4. Cross-talk, Selectivity, Reproducibility, and Stability of DIDμEs Immunosensors

The relevant cross-talking between the target proteins and noncognate proteins was evaluated on the neighboring modified

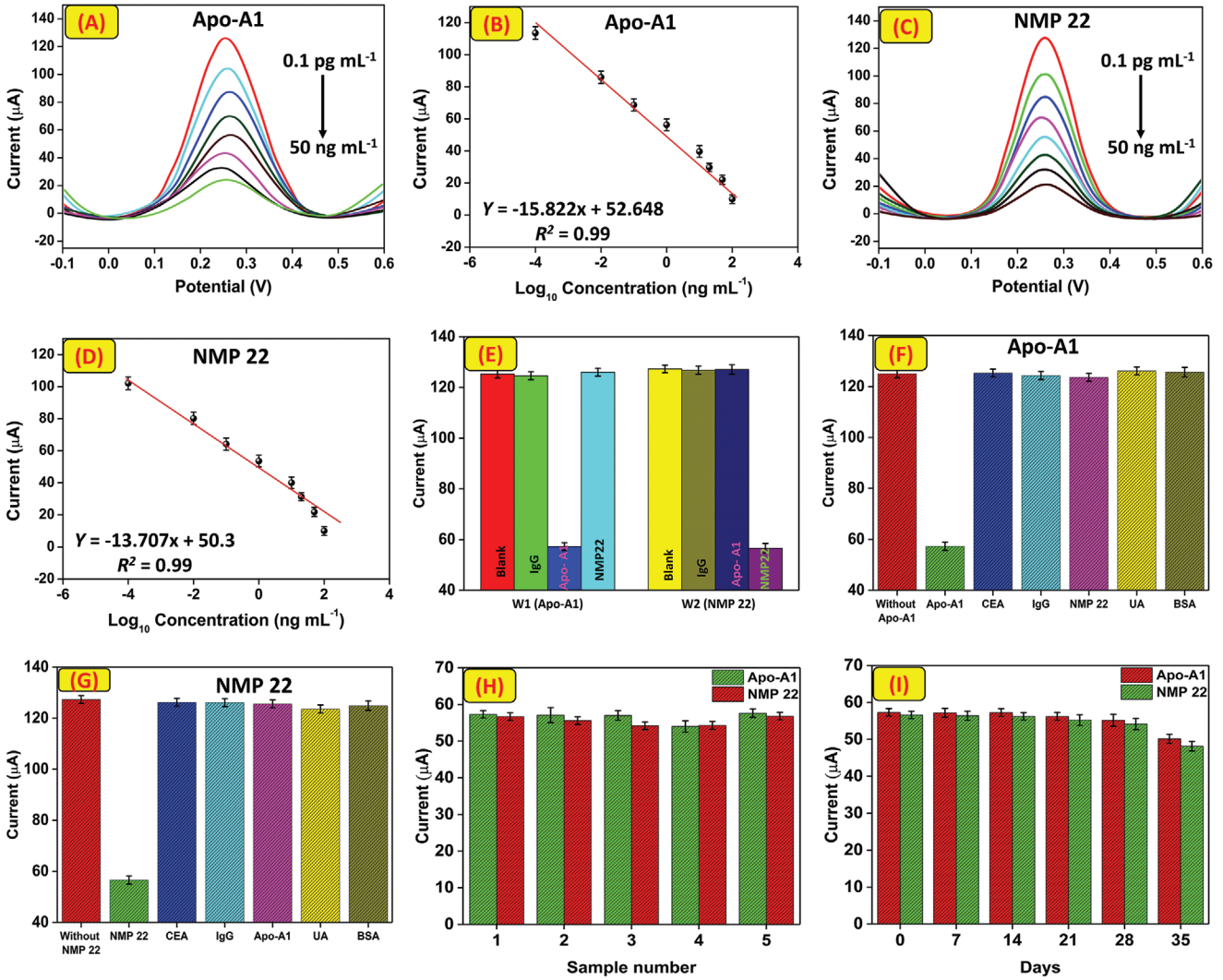

Figure 6. A) DPV response for Apo-A1 (W1) detection at different concentrations of Apo-A1 (0.1 pg mL^{-1}–50 ng mL^{-1}) in PBS (pH 7.4) containing 5.0 mM k_3/K_4 redox solution. B) Corresponding calibration plot for Apo-A1. C) DPV response for NMP 22 (W2) detection at different concentrations of NMP 22 (0.1 pg mL^{-1} to 50 ng mL^{-1}) in PBS (pH 7.4) containing 5.0 mM k_3/K_4 redox solution. D) Corresponding calibration plot for NMP 22. E) Cross-talk analysis of the dual immunosensor for W1 and W2. F) Selectivity measurement for the W1 (Apo-A1) electrode against various interferents. G) Selectivity measurement for the W2 (NMP 22) electrode against various interferents. H) Reproducibility test of the dual immunosensor. I) Stability test of the dual immunosensor.

Table 1. Determination of Apo-A1 in human urine samples using the fabricated immunosensor (W1).

Urine sample [ng mL^{-1}]	Added concentration [ng mL^{-1}]	Detected concentration [ng mL^{-1}]	Average concentration [ng mL^{-1}]	RSD [%]	Recovery [%]
0.5	5	5.63, 5.80, 5.76	5.73	1.55	104.1
	15	15.81, 14.90, 15.90	15.53	3.56	100.1
	20	18.06, 20.60, 20.86	19.84	7.8	96.78

W1 (immunosensor for Apo-A1 determination) and W2 (immunosensor for NMP 22 determination) surfaces by measuring the DPV currents on both immunosensors incubated with target proteins, a blank solution, and noncognate proteins with 10× higher concentration. Both Apo-A1 and NMP 22 immunosensors demonstrated clear DPV responses only toward their associated proteins (Figure 6E), implying the successful fabrication of cross-talk-free immunosensors for the simultaneous detection of Apo-A1 and NMP 22 in a single test.

The presence of different noncognate proteins in real samples may deteriorate the validity and practicability of the developed immunosensors. Therefore, a selectivity test was performed by comparing the DPV currents for 1 ng mL^{-1} of Apo-A1 and NMP 22 against other possible noncognate proteins, such as HER2, MUC1, AA, UA, and BSA with 50× higher concentrations. The results from the plotted bar graphs (Figure 6F,G) validate the high specificity and selectivity of the developed immunosensors toward only Apo-A1 and NMP 22. The DPV peak current variation owing to noncognate proteins was the same as those of the immunosensors without Apo-A1 and NMP 22.

Generally, reproducibility is an important factor in the practical application of any immunosensor. Hence, the reproducibility of the developed DIDμE immunosensors was assessed on five individual dual electrodes by detecting the DPV currents of 1 ng mL^{-1} of Apo-A1 and NMP 22 individually under ideal conditions. The obtained relative standard deviation (RSD%) from the bar graphs plotted for Apo-A1 and NMP 22 was 3.26% and 3.39% (Figure 6H), respectively, suggesting satisfactory reproducibility features of the developed DIDμE immunosensors.[47,48]

The long-term stability of MXNS-based immunosensors remains challenging owing to the oxidation of $Ti_3C_2T_x$ over time in liquid or humid air. Therefore, the storage stability of the developed DIDμE immunosensors was verified by detecting the DVP currents of 1 ng mL^{-1} of Apo-A1 and NMP 22 individually under optimal conditions (Figure 6I). Up to five weeks, over 95% of the initial DPV responses remained for both Apo-A1 and NMP 22, revealing the long-term self-lifetime of the DIDμE immunosensors.[45]

2.3.5. Analysis of Human Urine Samples

To investigate the analytical feasibility and reliability of the developed DIDμE immunosensors for potential clinical applications, a standard addition method was employed to identify the real recoveries of various concentrations of spiked Apo-A1 and NMP 22 in human urine samples (**Tables 1** and **2**). The recovery ranges of Apo-A1 and NMP 22 were 104.1–96.78% and 103.1–101.6%, respectively, demonstrating the reliability and practicability of the developed DIDμE immunosensors.

3. Conclusion

In summary, we demonstrated that MXNSs can be precisely and uniformly deposited on different sensing electrodes at room temperature within a few minutes via electroMXenition using a DMSO suspension with colloidal Ti_3C_2 nanosheets as an electrolyte. DMSO is a unique electrolyte for electroMXenition because MXNSs disperse completely and is highly stable in this organic solvent. We demonstrated that the precise uniformity of MXNSs on DIDμEs and ITO was achievable within 3 min at room temperature by varying the electroMXenition parameters optimally. Furthermore, a multifunctional TSIL, that is, AFBPB, was newly synthesized and implemented onto MXNSs to fabricate a label-free dual immunosensing platform. The resulting MXNSs-AFBPB-film-modified DIDμE label-free biosensor demonstrated a 7× higher redox current than bare electrodes owing to the uniform and specific deposition of conducting MXNSs and AFBPB. Under optimized conditions, the proposed dual immunosensor demonstrated a wide linear response range (0.1 pg mL^{-1} to 50 ng mL^{-1}), lower detection limits (0.3 pg mL^{-1} and 0.7 pg mL^{-1}), excellent selectivity, good reproducibility, and acceptable practicability in the human urine for Apo-A1 and NMP 22 detections, respectively, which satisfied clinical requirements. This versatile solution-based electroMXenition technique enables the deposition of low-cost, large-area, and high-quality MXNSs onto conductive electrodes, which is applicable to not only biosensing, but also electronics, optoelectronics, catalysis, and renewable energy.

4. Experimental Section

Chemicals and Apparatus: Explained in the Supporting Information.

Synthesis of MXNSs ($Ti_3C_2T_x$): MXNSs ($Ti_3C_2T_x$) were synthesized using the optimized MILD method, which involved the particular etching of aluminum layers from its pristine MAX phases (Ti_3AlC_2)

Table 2. Determination of NMP 22 in human urine samples using the fabricated immunosensor (W2).

Urine sample [ng mL^{-1}]	Added concentration [ng mL^{-1}]	Detected concentration [ng mL^{-1}]	Average concentration [ng mL^{-1}]	RSD [%]	Recovery [%]
1.0	5	6.18, 6.08, 6.30	6.18	1.78	103.1
	10	11.20, 11.32, 11.06	11.19	1.16	101.7
	20	21.43, 21.41, 21.20	21.34	0.60	101.6

(Figure 2A).[2] First, 0.6 g of LiF was gently added to 8 mL of 9 M HCl; subsequently, the etchant solution was stirred for 10 min, followed by the addition of 0.3 g of Ti_3AlC_2 powder gradually and allowing it to run for 24 h. The acidic solution was rinsed frequently with deionized H_2O (DI) via centrifugation (7000 rpm per 10 min cycle) for multiple times until its pH neutralized to ≈(6–7). After that, the collected dark black supernatant was dispersed in DI H_2O and ice bath sonicated for 1 h to delaminate the MXNSs, followed by 10 min centrifugation (10 000 rpm). Finally, the stable black MXNSs were extracted by centrifugation and dried for 36 h at 40 °C using a vacuum oven to obtain fine powder.

Synthesis of AFBPB TSIL: The synthesis procedure for multifunctional AFBPB is shown in Figure 2B. While stirring the solution of acetonitrile (5 mL), 4-aminopyridine (0.047 g, 0.5 mM), and 4-(bromomethyl)-benzaldehyde (0.099 g, 0.5 mM) were sequentially added, forming a colorless mixture, which was refluxed for 15 h at 80 °C. Subsequently, ethyl acetate was used as an anti-solvent to recrystallize and purify the turbid mixture from acetonitrile. Finally, separating the supernatant by filtering, the obtained white precipitate was dried (yield 0.12 g) and dispersed into ethanol for further use.

Fabrication of DIDμEs: The fabrication steps of DIDμEs by standard single-masked UV photolithography and etching procedures for sensor patterning and designing are schematically illustrated in Figure 1B. Briefly, a positive tone photoresist (PR; GRX 601) was spin coated at 500 rpm for 5 s followed by 3000 rpm for 30 s onto the surface of SiO_2/Au and soft baked at 95 °C for 120 s. Subsequently, a pattern-designed chrome mask with 190 IDE fingers (width = 10 μm, thickness = 2 μm, and gap = 5 μm) was transferred onto the PR coated substrate through UV light (365 nm) exposure. The UV-exposed SiO_2/Au substrate was dipped into a developer (AZ 3000MIF) for ≈60 s to develop a negative pattern of the patterned mask; subsequently, it was cleaned vigorously with DI water followed by a hard bake at 110 °C for 10 min. Finally, the PR-patterned SiO_2/Au substrate was dipped and shaken gently in an Au etchant for 20–30 s, which resulted in the formation of DIDμEs on the substrate.

Fabrication of Dual Immunosensors: The different steps included in the fabrication of the dual immunosensor (W1: Apo-A1 and W2: NMP 22) are schematically illustrated in Figure 2D. First, MXNSs were deposited onto specific IDEs of both W1 and W2 via electroMXenition, as mentioned in the Experimental Section. An aliquot (5 μL) from the as-prepared suspensions of AFBPB (5 mg mL^{-1}), a multifunctional TSIL, was then loaded on the surfaces of W1 and W2. AFBPB and the MXNSs bonded with each other through π–π and electrostatic absorption, which enabled a direct immobilization of antibodies Apo-A1 and NMP 22 without any coupling agent. Subsequently, 5.0 μL of 1 ng mL^{-1} anti-Apo-A1 and anti-NMP 22 antibodies were directly pipetted onto both working interfaces W1 and W2, respectively, and were incubated for 50 min at 4 °C. Next, the electrodes were carefully washed by BSA suspensions to remove unspecific binding molecules. Finally, to form a complete immunosensor array, both electrodes were incubated for 40 min with different concentrations of Apo-A1 (W1) and NMP 22 (W2) followed by washing with PBS to remove unbound sites.[46,49]

Supporting Information

Supporting Information is available from the Wiley Online Library or from the author.

Acknowledgements

This work was supported by the Bio & Medical Technology Development Program of the NRF grant funded by the Korean government (MSIT) (NRF-2017M3A9F1031270). Furthermore, the authors are grateful to the members of the ASER (Advanced Sensor and Energy Research Laboratory) group for their technical support and discussion.

Conflict of Interest

The authors declare no conflict of interest.

Keywords

4-amino-1-(4-formyl-benzyl) pyridinium bromide, bladder cancer analytes (Apo-A1 and NMP 22), dual interdigitated microelectrodes, electroMXenition, multiplexed immunosensors

Received: April 21, 2020
Revised: July 20, 2020
Published online:

[1] M. Naguib, M. Kurtoglu, V. Presser, J. Lu, J. Niu, M. Heon, L. Hultman, Y. Gogotsi, M. W. Barsoum, *Adv. Mater.* **2011**, *23*, 4248.
[2] M. Alhabeb, K. Maleski, B. Anasori, P. Lelyukh, L. Clark, S. Sin, Y. Gogotsi, *Chem. Mater.* **2017**, *29*, 7633.
[3] B. Anasori, M. R. Lukatskaya, Y. Gogotsi, *Nat. Rev. Mater.* **2017**, *2*, 16098.
[4] B. Akuzum, K. Maleski, B. Anasori, P. Lelyukh, N. J. Alvarez, E. C. Kumbur, Y. Gogotsi, *ACS Nano* **2018**, *12*, 2685.
[5] G. Gao, A. P. O'Mullane, A. Du, *ACS Catal.* **2017**, *7*, 494.
[6] Q. Jiang, N. Kurra, M. Alhabeb, Y. Gogotsi, H. N. Alshareef, *Adv. Energy Mater.* **2018**, *8*, 1703043.
[7] H. Tang, Q. Hu, M. Zheng, Y. Chi, X. Qin, H. Pang, Q. Xu, *Prog. Nat. Sci. Mater. Int.* **2018**, *28*, 133.
[8] H. Kim, Z. Wang, H. N. Alshareef, *Nano Energy* **2019**, *60*, 179.
[9] S. Kumar, Y. Lei, N. H. Alshareef, M. A. Quevedo-Lopez, K. N. Salama, *Biosens. Bioelectron.* **2018**, *121*, 243.
[10] L. Wu, X. Lu, Dhanjai, Z.-S. Wu, Y. Dong, X. Wang, S. Zheng, J. Chen, *Biosens. Bioelectron.* **2018**, *107*, 69.
[11] L. Liu, Y. Wei, S. Jiao, S. Zhu, X. Liu, *Biosens. Bioelectron.* **2019**, *137*, 45.
[12] H. Gu, Y. Xing, P. Xiong, H. Tang, C. Li, S. Chen, R. Zeng, K. Han, G. Shi, *ACS Appl. Nano Mater.* **2019**, *2*, 6537.
[13] Y. Zhang, X. Jiang, J. Zhang, H. Zhang, Y. Li, *Biosens. Bioelectron.* **2019**, *130*, 315.
[14] E. Ahn, T. Lee, M. Gu, M. Park, S. H. Min, B. Kim, *Chem. Mater.* **2017**, *29*, 69.
[15] Y. Si, J. W. Park, S. Jung, G. S. Hwang, E. Goh, H. J. Lee, *Biosens. Bioelectron.* **2018**, *121*, 265.
[16] K. Matsuba, C. Wang, K. Saruwatari, Y. Uesusuki, K. Akatsuka, M. Osada, Y. Ebina, R. Ma, T. Sasaki, *Sci. Adv.* **2017**, *3*, e1700414.
[17] B. Derby, *Annu. Rev. Mater. Res.* **2010**, *40*, 395.
[18] H. Tang, C. Yang, Z. Lin, Q. Yang, F. Kang, C. P. Wong, *Nanoscale* **2015**, *7*, 9133.
[19] G. Eda, G. Fanchini, M. Chhowalla, *Nat. Nanotechnol.* **2008**, *3*, 270.
[20] A. Sinha, Dhanjai, H. Zhao, Y. Huang, X. Lu, J. Chen, R. Jain, *TrAC Trends Anal. Chem.* **2018**, *105*, 424.
[21] Q. Chen, D. Liu, L. Lin, J. Wu, *Sens. Actuators B* **2019**, *286*, 591.
[22] L. Chen, Y. Tang, K. Wang, C. Liu, S. Luo, *Electrochem. Commun.* **2011**, *13*, 133.
[23] Q. Zhou, Q. Xie, Y. Fu, Z. Su, X. Jia, S. Yao, *J. Phys. Chem. B* **2007**, *111*, 11276.
[24] X. Wan, K. Chen, Z. Chen, F. Xie, X. Zeng, W. Xie, J. Chen, J. Xu, *Adv. Funct. Mater.* **2017**, *27*, 1603998.
[25] K. Maleski, V. N. Mochalin, Y. Gogotsi, *Chem. Mater.* **2017**, *29*, 1632.
[26] P. Nayak, Q. Jiang, R. Mohanraman, D. Anjum, M. N. Hedhili, H. N. Alshareef, *Nanoscale* **2018**, *10*, 17030.
[27] S. Tang, G. A. Baker, H. Zhao, *Chem. Soc. Rev.* **2012**, *41*, 4030.

[28] F. Ghorbanizamani, S. Timur, *Anal. Chem.* **2018**, *90*, 640.
[29] M. J. Trujillo-Rodríguez, H. Nan, M. Varona, M. N. Emaus, I. D. Souza, J. L. Anderson, *Anal. Chem.* **2019**, *91*, 505.
[30] Y. Shen, G. Shen, Y. Zhang, *Anal. Methods* **2018**, *10*, 1612.
[31] D. Manoj, K. Theyagarajan, D. Saravanakumar, S. Senthilkumar, K. Thenmozhi, *Biosens. Bioelectron.* **2018**, *103*, 104.
[32] Y. Shen, G. Shen, Y. Zhang, C. Zhang, H. Li, *Talanta* **2017**, *175*, 347.
[33] Z. Han, F. Li, J. Shu, L. Gao, X. Liu, H. Cui, *ACS Appl. Mater. Interfaces* **2016**, *8*, 17454.
[34] X. Yang, X. Zhang, Z. Liu, Y. Ma, Y. Huang, Y. Chen, *J. Phys. Chem. C* **2008**, *112*, 17554.
[35] R. Gondosiswanto, D. B. Hibbert, Y. Fang, C. Zhao, *Anal. Chem.* **2018**, *90*, 3950.
[36] R. D. Cowling, H. E. Hintermann, *J. Electrochem. Soc.* **1971**, *118*, 1912.
[37] B. Ahmed, D. H. Anjum, M. N. Hedhili, Y. Gogotsi, H. N. Alshareef, *Nanoscale* **2016**, *8*, 7580.
[38] J. Liu, X. Jiang, R. Zhang, Y. Zhang, L. Wu, W. Lu, J. Li, Y. Li, H. Zhang, *Adv. Funct. Mater.* **2019**, *29*, 1807326.
[39] M. Naguib, M. Kurtoglu, V. Presser, J. Lu, J. Niu, M. Heon, L. Hultman, Y. Gogotsi, M. W. Barsoum, *Adv. Mater.* **2011**, *23*, 4248.
[40] Q. Xue, H. Zhang, M. Zhu, Z. Pei, H. Li, Z. Wang, Y. Huang, Y. Huang, Q. Deng, J. Zhou, S. Du, Q. Huang, C. Zhi, *Adv. Mater.* **2017**, *29*, 1604847.
[41] X. Chen, X. Sun, W. Xu, G. Pan, D. Zhou, J. Zhu, H. Wang, X. Bai, B. Dong, H. Song, *Nanoscale* **2018**, *10*, 1111.
[42] S. J. Kim, H.-J. Koh, C. E. Ren, O. Kwon, K. Maleski, S.-Y. Cho, B. Anasori, C.-K. Kim, Y.-K. Choi, J. Kim, Y. Gogotsi, H.-T. Jung, *ACS Nano* **2018**, *12*, 986.
[43] Q. X. Xia, J. Fu, J. M. Yun, R. S. Mane, K. H. Kim, *RSC Adv.* **2017**, *7*, 11000.
[44] R. J. Toh, C. C. Mayorga-Martinez, Z. Sofer, M. Pumera, *Adv. Funct. Mater.* **2017**, *27*, 1604923.
[45] X.-H. Li, L. Dai, Y. Liu, X.-J. Chen, W. Yan, L.-P. Jiang, J.-J. Zhu, *Adv. Funct. Mater.* **2009**, *19*, 3120.
[46] M. Sharifuzzaman, S. C. Barman, M. A. Zahed, N. J. San, J. Y. Park, *J. Electrochem. Soc.* **2019**, *166*, B249.
[47] S.-E. Kim, Y. J. Kim, S. Song, K.-N. Lee, W. K. Seong, *Sens. Actuators B* **2019**, *278*, 103.
[48] S. Zhao, Y. Zhang, S. Ding, J. Fan, Z. Luo, K. Liu, Q. Shi, W. Liu, G. Zang, *J. Electroanal. Chem.* **2019**, *834*, 33.
[49] M. Sharifuzzaman, S. C. Barman, M. T. Rahman, M. A. Zahed, X. Xuan, J. Y. Park, *J. Electrochem. Soc.* **2019**, *166*, B983.